To be published in Journal of Optical Communications and Networking:

Title: (OFC 2024) Overview on State of Polarization Sensing: Application Scenarios and Anomaly Detection Algorithms

Authors: Saverio Pellegrini,Leonardo Minelli,Lorenzo Andrenacci,Giuseppe Rizzelli Martella,Dario Pilori,Gabriella Bosco,Luca Della Chiesa,Claudio Crognale,Stefano Piciaccia,Roberto Gaudino

Accepted: 26 November 24

Posted 06 December 24

DOI: https://doi.org/10.1364/JOCN.537881

Overview on State of Polarization Sensing: Application Scenarios and Anomaly Detection Algorithms

SAVERIO PELLEGRINI,[1,*] LEONARDO MINELLI,[1] LORENZO ANDRENACCI,[1] GIUSEPPE RIZZELLI,[1] DARIO PILORI,[1] GABRIELLA BOSCO,[1] LUCA DELLA CHIESA,[2] CLAUDIO CROGNALE,[2] STEFANO PICIACCIA,[2] AND ROBERTO GAUDINO,[1]

[1]*Dipartimento di Elettronica e Telecomunicazioni, Politecnico di Torino, Torino, Italy.*
[2]*Cisco Photonics Italy, Vimercate, Italy.*
[*]*saverio.pellegrini@polito.it*

Abstract: Given the ubiquity of optical fiber networks in both terrestrial and submarine environments, leveraging these facilities for sensing anomalous conditions alongside telecommunications can provide significant added value. In this context, distributed acoustic sensing (DAS) systems have been widely employed and discussed, due to their sensitivity and ability to locate events. However, integrating them within existing networks is complex and expensive. On the other hand, the received state of polarization (SOP) is also sensitive to external factors and it can be used for sensing: in this case, no extra hardware would be required since the SOP is already estimated in coherent receivers for data demodulation. The sensing information is provided "for free" by the already installed hardware, potentially requiring only a software upgrade. In this work, we analyze the feasibility of using polarization-based sensing to detect anomalous conditions in metropolitan environments. A polarimeter was used to evaluate SOP noise induced by urban factors, while a commercial coherent transceiver was employed to assess SOP estimation noise. We propose two algorithms for processing polarization data: a time-based method called SOP angular speed (SOPAS) and an adaptive, frequency-based approach named SOP-Power Spectral Density Gap (SOP-PSDG). These algorithms were compared by processing Stokes vector samples from the polarimeter when different sinusoidal vibrations are applied to the fiber, through a mechanical shaker. Results demonstrate that a sampling rate of just a few tens of Hz is sufficient to effectively identify various hazardous conditions, with SOP-PSDG consistently outperforming SOPAS. Additionally, preliminary findings on the performances of these algorithms using SOP samples from a commercial coherent receiver are discussed.

1. Introduction

In recent years, given the widespread installation of optical fiber networks in terrestrial and submarine scenarios, there has been an increasing research interest in using pre-installed optical fiber infrastructures to monitor the external environment. Various events could pose a risk not only to the fiber cables themselves but also to people's safety and infrastructure's integrity. Distributed fiber sensing techniques are experiencing increasing growth, especially in the last years, given their sensitivity to mechanical perturbations coming from the fiber cable's surroundings, and possibly anticipating dangerous conditions to which early warning would be necessary. For geophysical and civil engineering applications, Brillouin-based sensing and Rayleigh-based Distributed Acoustic Sensing (DAS) are the two main techniques, sensitive to mechanical stresses and temperature variations [1, 2]. The working principle is the same for both of them: light backscattering is exploited to sense and locate any condition generating axial strain on the fiber. Among the two, DAS-based systems are finding the largest appreciation for metropolitan monitoring [3, 4] and earthquake detection [5–7], thanks to their ability to detect dynamic events, such as mechanical vibrations up to the kHz range. DAS systems have proven to deliver

outstanding results, particularly among the geophysics community, given the optical fibers' unrivaled spread, especially in submarine environments where they are the only medium lying on the ocean seafloor that can be used as a sensor. For this reason, there is a growing interest in merging their data transmission capabilities with their sensing ones. Monitoring the metropolitan environment is also fundamental in providing early warnings for conditions jeopardizing the optical fiber networks' health status, such as fiber cuts. To ensure good compatibility between telecommunication fiber systems and sensing, DAS can be a viable solution [8, 9], but some concerns need to be addressed. Firstly, DAS is limited in sensing distance by both the amount of backscattered power, which lowers the sensing range to around 100 km, and by the presence of optical amplifiers that include isolators (e.g. EDFAs), which completely block light backscattering. The use of properly engineered "dark fibers" would ease the former, but they do not match the fiber type already installed for telecommunication applications. Secondly, narrow linewidth lasers [10, 11] are not part of the usual commercial coherent transceivers, but are essential for the proper functioning of DAS systems. Additionally, the amount of data generated is huge: since they are resolved in time and space, the stream generated would be complex to manage and could represent an actual bottleneck to real-time early warning for hazardous conditions. For these reasons, integrating DAS with the existing telecommunication infrastructure may not be cost-effective in most cases.

In this context, an alternative approach might be to monitor the light's optical phase or state of polarization (SOP) at the receiver side [12]. However, since both techniques are length-integrated and based on forward transmission, they do not rely on backscattering, making accurate event localization more challenging. On the other side, the sensing distance is not limited by low back-reflected power, or by EDFAs isolators, allowing for much higher ranges. Regarding phase sensing, several works demonstrated its reliability in monitoring earthquakes in submarine [13] and terrestrial [14–18] environments, proposing algorithms to resolve events localization, particularly over long-haul links [19]. Research has been conducted to adapt coherent transceivers in processing data for sensing applications [20]. Despite the reliability achieved by optical phase sensing, the system requirements do not match the usual equipment used for telecommunications by coherent transceivers, since phase sensing requires ultra-narrow linewidth lasers. Cost-efficiency would then again be compromised, as the already installed telecommunication hardware could not be exploited as it is.

State of polarization monitoring [21–29] can be used as an alternative technique to optical phase monitoring. Geometrical deformations [30, 31], mechanical stresses, and vibrations [32–34], due to the photoelastic effect, change the dielectric tensor of glass [35,36], inducing fiber birefringence and affecting light polarization at its output. Sensitivity to the agents mentioned above has been demonstrated in various works in both the submarine [37,38] and the terrestrial [23] environments. Since standard coherent receivers already need to estimate the polarization state to perform data demodulation, the sensing-related information would thus be obtained almost completely "for free" [20, 39, 40], provided that a transceiver input/output monitoring channel delivering SOP data and a software capable of processing them in real-time are made available. Moreover, the amount of data to process is also limited since no space resolution is available, as opposed to the DAS.

The work presented in this manuscript is an invited extension of [41], which also builds upon our previous research [42, 43]. We focus on a possible implementation of a polarization-based sensing system in a metropolitan environment, able to provide fast real-time alarms whenever an anomalous condition, possibly due to hazards, is detected. This discussion will cover the practical feasibility of SOP-based sensing, including the required digital signal processing, experimental demonstrations, and resulting detection performance. In Section 2 we will discuss SOP data extraction from coherent receivers, focusing on the accuracy of the estimates and the associated sampling speed. Once we establish the baseline conditions required for polarization

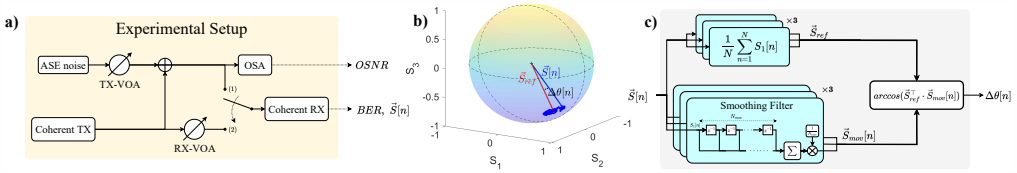

Fig. 1. (a) experimental setup. When connection (1) is selected, the coherent RX considers ASE noise injected in the system. When instead connection (2) is selected, ASE noise is excluded. (b) Poincaré sphere showing the $\vec{S}_{ref}$ (in red) and $\vec{S}[n]$ (in blue) vectors and the angular deviation $\Delta\theta[n]$. (c) Post-processing scheme exploited to compute the angular deviation $\Delta\theta[n]$. A long-term average of N samples over the whole $\vec{S}[n]$ time series is employed to obtain $\vec{S}_{ref}$ vector. A smoothing filter is applied over each single Stokes parameter time evolution to obtain instead $\vec{S}_{mov}[n]$. The last block shows how the angular deviation $\Delta\theta$ is computed.

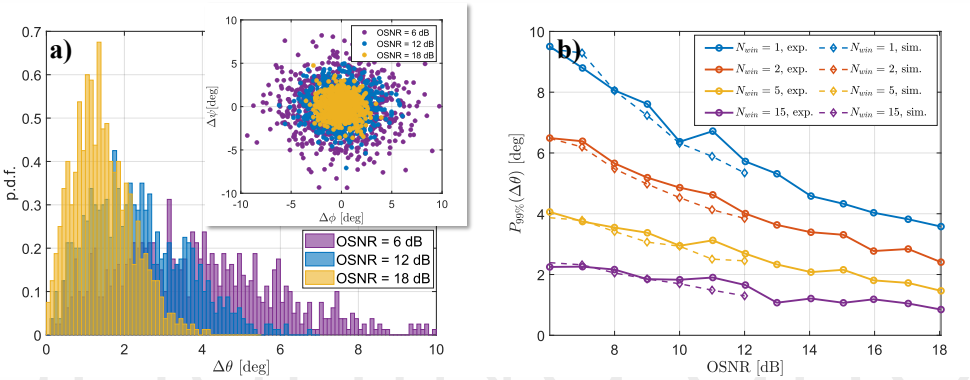

Fig. 2. (a) $\Delta\theta[n]$ histograms at three different OSNR levels. The inset reports the cloud distribution of the SOP points over the Poincaré sphere surface, in angular coordinates. (b) $P_{99\%}(\Delta\theta)$ vs. OSNRs for different moving average windows N_{win} (experiments and numerical simulation).

data extraction, Section 3 will detail the state of polarization noise induced by the metropolitan environment, where the experiments in Section 4 have been carried out, simulating hazardous conditions that could potentially jeopardize the health of metropolitan fiber networks. Section 5 will introduce and propose SOP-based signal processing algorithms. Section 6 will compare their detection performance under hazardous conditions. Final observations and conclusions will be presented in Section 7.

2. Accuracy of state of polarization estimate from coherent receivers' DSP

This section experimentally examines the physical layer parameters that influence the accuracy of SOP estimation using standard coherent transceivers. The experiments detailed herein utilize a commercial transceiver capable of providing the received light SOP estimate through its internal receiver DSP (a typical scenario for SOP-based sensing). In the following, we assess the accuracy of the SOP estimate over different system conditions:

1. **Performance limited by ASE noise**: employing ASE noise loading, this scenario emulates long-haul optically amplified transmissions with sufficiently high received optical power (ROP). Results will be presented for different values of optical signal-to-noise ratio (OSNR).

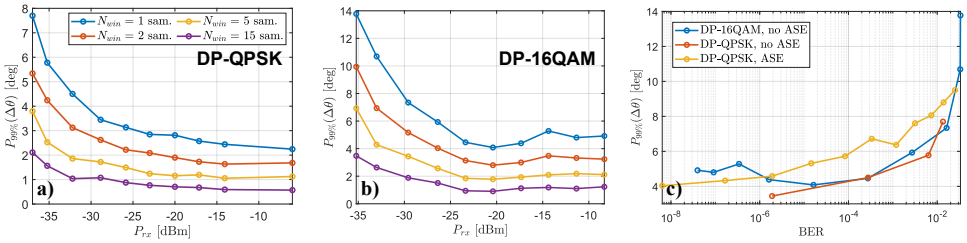

Fig. 3. $P_{99\%}(\Delta\theta)$ vs. ROP for (a) DP-QPSK and (b) DP-16QAM, using different averaging windows. Legend in (a) applies also in (b). (c) $P_{99\%}(\Delta\theta)$ vs. BER levels in all the considered situations, with $N_{\text{win}} = 1$.

2. **Performance limited by the ROP**: this scenario emulates short-reach, non-optically amplified single-span systems, with no ASE noise and low ROP, using either DP-QPSK or DP-16QAM modulation.

A scheme of the experimental transmission system is shown in Fig. 1(a). To avoid stress-induced birefringence and geometrical deformations, all the fiber cords were fixed on a stable optical bench, ensuring a nominally constant received SOP. Conventionally, the Variable Optical Attenuators (VOA) have been named TX-VOA (transmitter side) and RX-VOA (receiver side). When performing experiments with ASE noise loading, the coherent receiver (RX) has been connected to the coherent transmitter (TX) through connection (1) in Fig. 1(a). On the contrary, in the experiments without ASE noise, the coherent RX has been connected to the coherent TX, cascaded with the RX-VOA, through connection (2). The commercial transceiver can output SOP samples at about 20 S/s, and record the related BER during the acquisition.

In parallel to the experiments, we also run time-domain simulations of the optical system, assuming a standard coherent RX [44] operating at 2 Samples/symbol, using an LMS-based 2×2 adaptive equalizer, with $N_{\text{tap}} = 16$ taps. The input signal $\boldsymbol{x}[n]$ and the output signal $\boldsymbol{y}[n]$ at this stage are related by $\boldsymbol{y}[n] = \boldsymbol{W}[n] \cdot \boldsymbol{x}[n]$, where n is the discrete time index and $\boldsymbol{W}[n]$ the equalization matrix defined in (1):

$$\boldsymbol{W}[n] = \begin{bmatrix} \boldsymbol{w}_{11}^{(m)}[n] & \boldsymbol{w}_{12}^{(m)}[n] \\ \boldsymbol{w}_{21}^{(m)}[n] & \boldsymbol{w}_{22}^{(m)}[n] \end{bmatrix} . \tag{1}$$

Here, m represents the tap index. Each element of the equalization matrix is an $N_{\text{tap}} \times 1$ vector, whose DC component is equal to $\bar{w}_{ij}^{(m)} = \sum_{m=1}^{N_{\text{tap}}} w_{ij}^{(m)}[n]$ with $i, j = 1, 2$. Note that the DC component of either column of $\boldsymbol{W}[n]$ is a Jones vector that can be used to compute the corresponding Stokes parameters, defined as (considering the first column of the matrix in (1)):

$$\begin{aligned} S_0[n] &= |\bar{w}_{11}[n]|^2 + |\bar{w}_{21}[n]|^2 \\ S_1[n] &= |\bar{w}_{11}[n]|^2 - |\bar{w}_{21}[n]|^2 \\ S_2[n] &= 2 \cdot \text{Re}(\bar{w}_{11}[n] \cdot \bar{w}_{21}^*[n]) \\ S_3[n] &= -2 \cdot \text{Im}(\bar{w}_{11}[n] \cdot \bar{w}_{21}^*[n]) . \end{aligned} \tag{2}$$

In (2), $(\cdot)^*$, $\text{Re}(\cdot)$ and $\text{Im}(\cdot)$ are the complex conjugation, real part, and imaginary part operators, respectively. In the following discussion, we will refer to the Stokes parameters using the normalized Stokes vector $\vec{S}[n] = [S_1[n], S_2[n], S_3[n]]$, where each element is normalized with respect to $S_0[n]$. We extracted the equalizer tap coefficients every 200 ns while processing a sequence of 20 million samples, leading to a SOP sampling frequency f_s of 5 MS/s. In all cases,

both experiments and simulations, the transmission is operated back-to-back at 34 GBaud (QPSK line rate is 100 Gbit/s, 16-QAM line rate is 200 Gbit/s), shaped with a square-root raised-cosine filter with roll-off $\rho = 0.2$.

To measure the SOP estimate accuracy, we evaluated the angular deviation of each Stokes vector with respect to a reference one. Figure 1(b) shows as blue dots the vector $\vec{S}[n]$ time evolution, extracted from the commercial coherent receiver, or numerical simulation equalizer. The red $\vec{S}_{ref}$ vector is the reference to compute the angular deviation, denoted as $\Delta\theta$. The post-processing algorithm is shown in Figure 1(c). Each parameter $S_1[n]$, $S_2[n]$, $S_3[n]$ is passed through a moving average filter (Smoothing filter in Fig. 1(c)), with filtering window length N_{win} ($N_{\text{win}} = 1$ samples is equivalent to no-filtering). The output of this block is a smoothed version of the input Stokes vector time evolution, denoted as $\vec{S}_{mov}[n]$. Each Stokes parameter of the whole $\vec{S}[n]$ acquisition is also averaged over a total number of N samples inside the acquisition (long-term average in Fig. 1(c)), with N in the order of a few hundred samples. The output of this block is $\vec{S}_{ref}$, in red in Fig. 1(b). This represents a "ground-truth" vector, placed at the center of the noise cloud over the Poincaré sphere surface. We remind that in this specific experiment, fiber birefringence was intentionally constant over time, thus the SOP variations are only due to the estimation noise generated inside the coherent receiver. The angular deviation $\Delta\theta[n] = \arccos(\vec{S}_{ref}^{\top} \cdot \vec{S}_{mov}[n])$ (right-most block in Fig. 1(c)), $(\cdot)^{\top}$ being the transposition operator, gives an insight into the noise condition, representing the spread of the SOP noise cloud [45].

2.1. Performance in ASE noise

In this scenario, the coherent RX goes through connection (1) in the experimental setup (see Fig. 1(a)), allowing for the TX-VOA to control the injection of ASE noise. The OSNR values, ranging between 6 dB and 18 dB, have been measured with the OSA, while SOP samples were returned from a commercial coherent transceiver as Stokes vector time evolution.

Fig. 2(a) shows the probability density functions (pdf) of $\Delta\theta[n]$ for three different values of OSNRs (6, 12 and 18 dB) for DP-QPSK modulation format and N_{win}=1. The inset in the Figure also shows the SOP cloud spread in angular coordinates (i.e., mapped over two orthogonal rotation axes). As expected, these histograms show that, for higher OSNR values, the statistical spread on the $\Delta\theta[n]$ pdf is smaller and, in a practical sensing system, mechanical stresses generating higher deviations would be easier to detect, since less blurred by noise. To quantitatively assess this consideration, we introduce the 99th percentiles of the angular deviation, i.e. the angle $P_{99\%}(\Delta\theta)$ at which the probability of $\Delta\theta[n]$ exceeding it is 1%. Since the angular deviation is always positive and the pdf are not symmetrical, this evaluation metric is more suitable in assessing the distribution spread than either the mean value and/or the standard deviation. Fig. 2(b) shows $P_{99\%}(\Delta\theta)$ vs. OSNR for different values of N_{win}. Circle-marked lines represent the experimental results, while the diamond-marked dashed lines represent the time-domain simulations, demonstrating an almost complete match between the "ideal" condition used in simulations and experiments. The presented results seem thus independent from the actual RX DSP implementation details. The diamond-marked dashed lines are limited to 12 dB, the highest OSNR value at which we could obtain reliable BER values ($\sim 10^{-4}$) through time-domain simulations, with a reasonable expense of numerical effort and running time. We observe that for increasing N_{win}, $P_{99\%}(\Delta\theta)$ decreases, going for instance below 2° for N_{win}=15, for all the measured OSNR values. The moving average introduced to evaluate $\vec{S}_{mov}[n]$ can be implemented with very limited additional DSP complexity and can thus be used to reduce the impact of SOP noise significantly. The only trade-off to be considered is that when increasing N_{win}, the effective sample rate in SOP estimation is reduced. Consider also that the mechanical events to be detected have quite low-frequency content (few Hz to few tens of Hz) [3, 4, 13, 39, 46]. This eases the need

for extremely fast and high-cost processing hardware and also for complex SOP data storage solutions.

2.2. Performance limited by low ROP (without ASE noise)

In this scenario, referring to the scheme in Fig. 2(a), connection (2) has been selected, thus excluding the ASE noise loading, the TX-VOA, and the OSA. The ROP value P_{rx} has been varied using the RX-VOA. Experiments have been repeated for DP-QPSK and DP-16QAM, with BER and SOP estimates always recorded at the coherent RX in each situation. The experimental results are shown in Fig. 3(a) and 3(b) in terms of $P_{99\%}(\Delta\theta)$ vs. P_{rx}, and show a similar trend to Fig. 2(b), so that the same system comments can be derived also for this ROP-limited situation and for the two different modulation formats considered here. Once again, averaging controlled by the N_{win} parameter confirms its strong impact on the accuracy, since it allows to lower the percentiles up to around 1° in the best cases.

Fig. 3(c) shows $P_{99\%}(\Delta\theta)$ as a function of the BER measured for the different considered ROP values at the output of the coherent receiver, when no smoothing is applied ($N_{\text{win}} = 1$). This represents a practical way to assess the SOP angular accuracy in commercial systems, since given a BER threshold set by the chosen FEC, it indicates the corresponding typical values of $P_{99\%}(\Delta\theta)$. Moreover, in Fig. 3(c), the blue and red curves show a high degree of overlap, suggesting that, in the absence of ASE noise, the relationship between $P_{99\%}(\Delta\theta)$ and BER is quite insensitive to the modulation format. Finally, it can be observed that the yellow $P_{99\%}$ curve in Fig. 3(c), corresponding to the situation in Subsection 2.2.1, is shifted above the others of around 1°, clearly indicating a significant impact of the ASE noise in the system.

3. SOP environmental noise in metropolitan fibers

When implemented on a metropolitan optical fiber cable, a polarization-based sensing system is inevitably influenced by the urban environment, which causes random SOP fluctuations (referred to in this work as *SOP environmental noise*). External factors such as temperature changes, traffic, and construction activities can induce fiber birefringence, resulting in SOP variations. This section shows how some of these factors can affect the SOP. Differently from Section 2, where a commercial coherent receiver was employed, all the following experiments were conducted using a commercial *polarimeter*. As the SOP sampling frequency of the available coherent receiver is fixed to 20 S/s by the internal telemetry system, it is not suitable to correctly characterize the dynamic metropolitan environment and detect malicious mechanical events producing vibrations at frequencies higher than about 10 Hz. On the other hand, the polarimeter allows for an arbitrary adjustment of the sampling frequency up to the MHz range and thus enables a more complete analysis of the proposed algorithms.

Figure 4 illustrates the experimental setup, which utilizes fiber cables deployed in the Turin metropolitan area, with their endpoints located in our laboratory. Specifically, we primarily used a 35-km fiber (green line in Fig. 4), while some experiments in Section 6 will also involve the 10-km fiber (red line in Fig. 4). The setup comprises an external cavity laser operating in continuous wave (CW) mode, with 0 dBm launch power and 100 kHz linewidth, and a Novoptel PM1000 polarimeter for acquiring the SOP at the other endpoint. The sampling frequency is set to 95.4 S/s, one of the f_s values available from the device, which is suitable for our purposes given the low-frequency ranges typically excited by the urban environment [4]. The SOP data are provided as the time evolution of normalized Stokes vectors.

To characterize the SOP environmental noise, we acquired the SOP evolution over the 35 km long metropolitan fiber in quiet conditions, without generating any external event. Figure 5(a) shows the evolution of the Stokes vector acquired for two days, starting from March 4$^{\text{th}}$, 2023. At first glance, the statistics of the Stokes parameters exhibit gradual hourly changes. These slow SOP variations generally exhibit a daily pattern: as shown in Figure 5(a), during

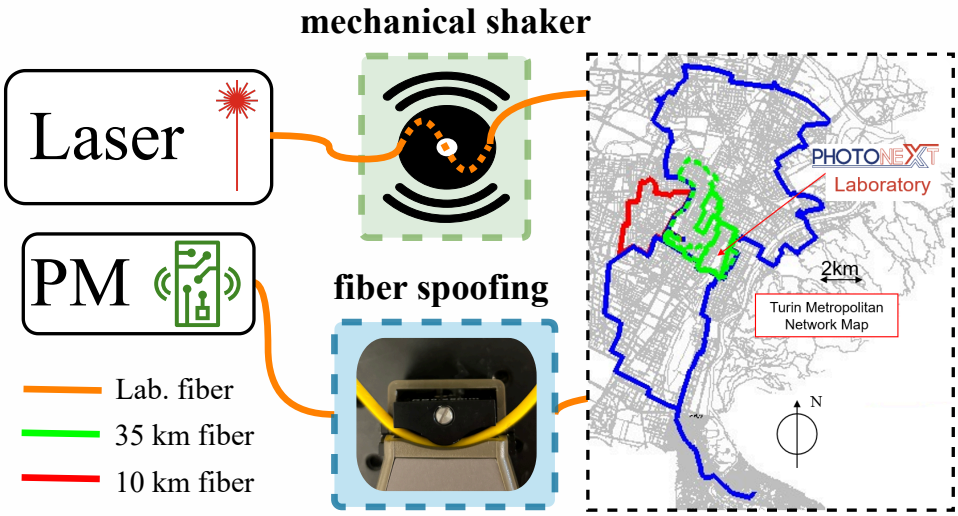

Fig. 4. Experimental set-up used for the experiments. The laboratory fiber is represented by the orange line. A mechanical shaker is applied to it (green-dashed block) before it enters the metropolitan ring while spoofing attempts (blue-dashed block) are generated just before the polarimeter. Green and red lines depict the fibers used for the experiments, running around Turin, measuring 35 km and 10 km, respectively. Blue line depicts a fiber that was not used for the experiments.

both March 4th and 5th, the SOP remains relatively stable around midnight, starting to deviate only a few hours before noon, likely due to increased human activities in the urban environment. When examining a shorter time window of a few tens of seconds (insets in Figure 5(a)), the SOP environmental noise becomes evident: the Stokes parameters display random fluctuations around their hourly-varying average values. On average, the recorded $P_{99\%}(\Delta\theta)$ value is 0.23°, which is lower than the ones obtained using a coherent receiver and discussed in Section 2.

The SOP fluctuation can be analyzed through the evaluation of the power spectral density (PSD) of S_1, S_2, and S_3. Figure 5(b-d) shows the evolution of the PSDs (i.e., the spectrogram) of the three Stokes parameters. The three PSDs exhibit several common features: a high-magnitude zero-frequency component (red lines at $f = 0$), consistently high magnitudes in the frequency range between 5 and 15 Hz, and an intense pure frequency component at 46 Hz. To comprehensively observe all the frequency components in the SOP noise, Figure 6 illustrates the spectrogram corresponding to the sum of the three PSDs over the same time window as in Figure 5(a). It can be clearly observed that this representation effectively captures the characteristics of the SOP noise, giving equal weight to each Stokes parameter and incorporating all the frequency components present in their relative spectra in Figure 5(b-d). Environmental agents indeed affect the Stokes parameters arbitrarily, depending on the current SOP. However, their contribution to the SOP spectrum remains consistent at specific frequencies, regardless of the direction the Stokes vector takes on the Poincaré sphere. This characteristic is exploited in the SOP-PSDG algorithm [42], which we will illustrate in Section 5.5.2. Additionally, as shown in Figure 6, certain intense low-frequency components (below 5 Hz) tend to be more intense around noon, corresponding with the daytime Stokes fluctuations observed in Figure 5(a). Conversely, the frequency range becomes less intense when reaching the nighttime hours.

Regarding the frequency components with significant magnitudes between 5 and 15 Hz, as

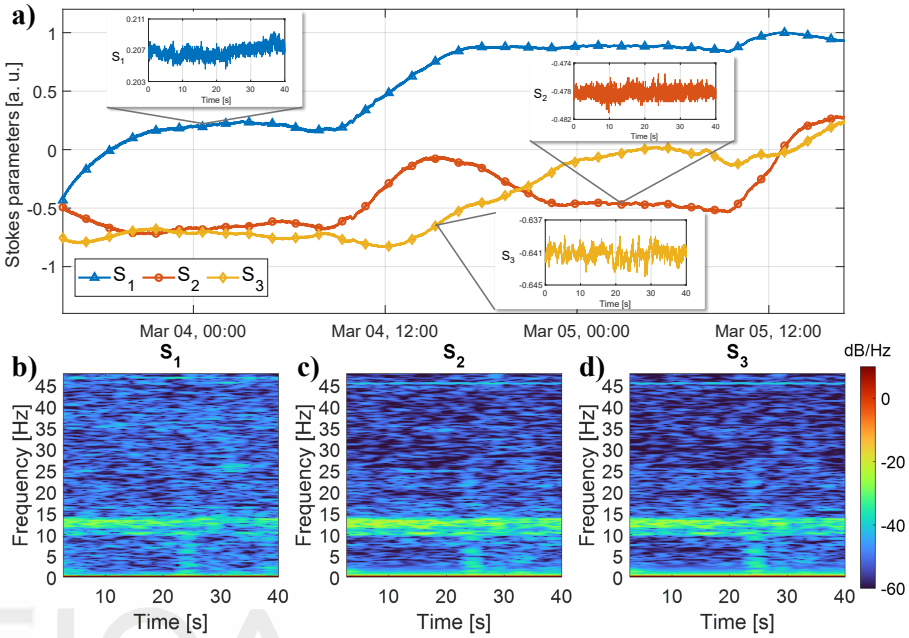

Fig. 5. (a) Stokes parameters time evolution over a two-days-long acquisition considering the 35 km long metropolitan fiber, started on March 4th 2023. Insets provide a 40 seconds zoom on one Stokes parameter, in different portions of the acquisition. (b-d) 40 seconds long spectrogram of the single Stokes parameters.

well as other higher-frequency tones that are less intense but almost perfectly constant, these do not appear to be caused by the urban environment. These frequency components are also observed when the metropolitan fiber is not part of the setup (i.e. when acquiring the SOP using only the optical fiber within the laboratory). The likely cause of this effect in the SOP spectrum is the presence of cooling fans near the optical fiber path, such as those in our laboratory. This condition is common in practical scenarios, such as central offices and data centers.

4. Anomalous conditions characterization

On top of the SOP environmental noise, characterized in the previous section, anomalous events affecting the optical fiber health status can generate SOP variations which can be analyzed both through angular deviation and SOP spectral analysis. These conditions will be discussed in the following subsections.

4.1. Mechanical vibrations

In the metropolitan scenario, fiber cuts and physical network infrastructure damages represent the most typical hazards. Maintenance or construction works, which usually employ excavators and jackhammers, can jeopardize the health of the underground fiber cables, with consequent re-installation costs and inconveniences for the vendors controlling the network services. Since the SOP is sensitive to mechanical stresses and geometrical deformations, the vibrations induced on the fiber before the occurrence of the actual damages could be used as an immediate early warning for potentially hazardous conditions.

In this analysis, we use a mechanical shaker to generate vibrations (green-dashed block in Fig. 4) over a portion of the laboratory fiber (in orange in Fig. 4), assuming that no abnormal condition

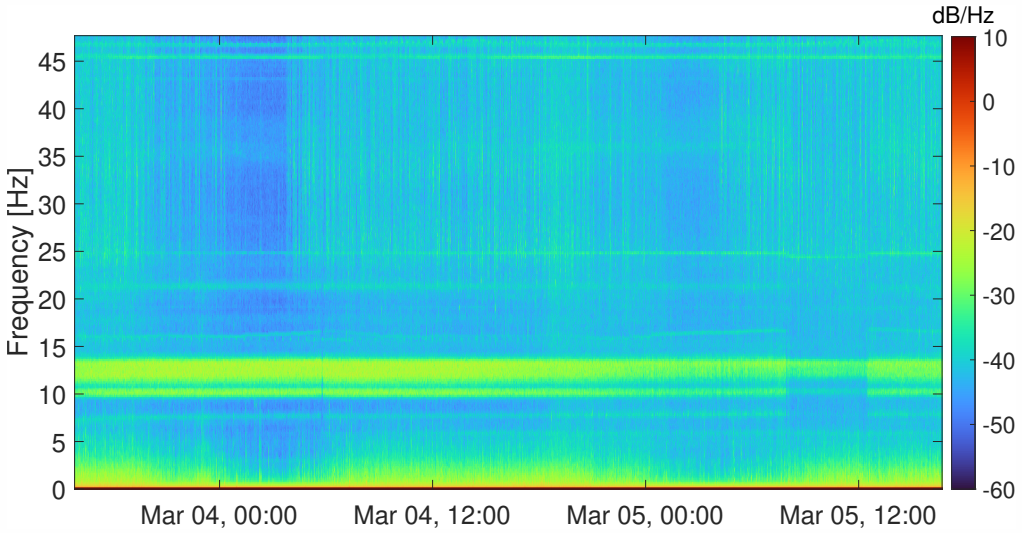

Fig. 6. Spectrogram of a 2-days acquisition over the 35 km long metropolitan fiber, obtained as the sum of the PSDs of the three Stokes parameters.

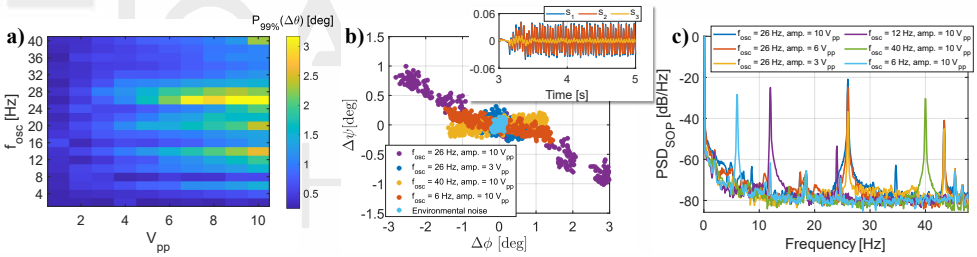

Fig. 7. (a) $P_{99\%}(\Delta\theta)$ values for different vibrations induced on the fiber, changing f_{osc} and V_{pp}. (b) angular coordinates plot showing the SOP cloud on the Poincaré sphere surface for different vibrations (purple, blue, yellow, orange dots), and for the environmental noise only (light blue dots), on the 35 km long metropolitan fiber. Inset shows the effect that vibration with f_{osc} = 26 Hz and amp. = 10 V_{pp} has on the Stokes parameters. (c) SOP PSDs for different vibrations induced on the fiber.

occurs on the 35-km metropolitan fiber during our tests. The laboratory fiber cable is a simplex standard single mode G.652 fiber patchcord with LSZH coating and 2mm diameter, while the rest of the metropolitan fiber uses standard telecom fiber cables, for which we do not have detailed information. Since fiber displacements, geometrical deformations, and stresses are generated during the experiments, they can be used to assess the effects that different vibrations of different intensities would have on the SOP. It should be pointed out that we will not accurately reproduce the effects that real-life maintenance works, jackhammers, or excavators [20] would have on the fiber before generating damages or cuts. The precise modeling of how they would couple on the fiber cable after ground propagation is out of the scope of this work. The mechanical shaker is driven by sinusoid signals generated by an analog waveform generator (AWG) and consists of a vibrating rectangular plastic plate, where one meter of fiber has been glued, oscillating in the vertical direction and generating a maximum displacement of 4mm. The oscillation frequency f_{osc} can be changed from the AWG, as well as its amplitude, expressed in peak-to-peak voltages, to which we will refer as V_{pp} units.

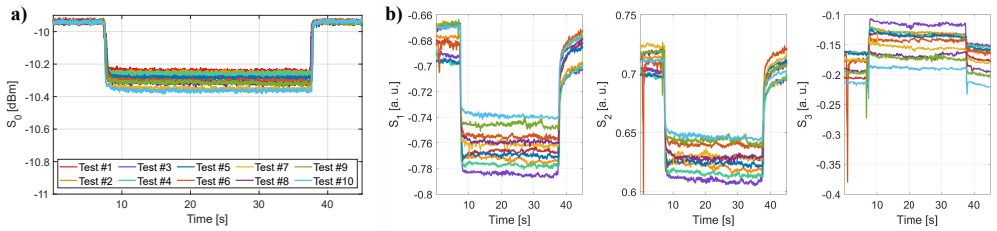

Fig. 8. Effect of fiber clamping on (a) the instantaneous power S_0, and (b) the SOP as Stokes parameters S_1, S_2, S_3. Legend in (a) applies also to all the plots reported in this figure.

We first characterize the vibrations by computing the angular deviation $\Delta\theta$ (consistently with what has been done in Section 2, but no smoothing has been applied in this case) of the SOP captured from the polarimeter, when the vibration is turned on. The map in Fig. 7(a) shows the values of $P_{99\%}(\Delta\theta)$ versus f_{osc} and V_{pp}. As previously mentioned in Section 3, the average value of $P_{99\%}(\Delta\theta)$ in quiet conditions is around 0.23°, thus shaker-induced angular deviations with similar values correspond to SOP variations comparable with environmental noise. In general, vibrations having amplitude higher than 6 V_{pp} and f_{osc} from around 12 Hz to 32 Hz seem to have non-negligible consequences on the SOP. The one generating the largest SOP variation occurs for f_{osc} values around 26 Hz with an amplitude of 10 V_{pp}. However, it should be noted that the intensity of mechanical vibrations on the attached fiber depends not only on the oscillation frequency and amplitude but also on the geometry and material properties of the plate. To better observe the effects of the vibration on the SOP, Fig. 7(b) shows a scatter plot of the Stokes vector angular coordinates for different vibrations. The light blue cloud at the center of the graph represents SOP environmental noise only. When a vibration with f_{osc} = 26 Hz and 10 $V_{pp}$is applied, it generates the largest spread (purple points in Fig. 7(b)), with a deviation of around 3° from the initial noise cloud, consistent with Fig. 7(a). Testing different f_{osc} and V_{pp} pairs results in reduced vibration-induced cloud spread (blue, yellow, orange).

Comparing these results to the ones illustrated in Section 2, it should be noted that mechanical oscillations yielding $P_{99\%}(\Delta\theta)$ values of 3°, i.e. the most intense generated in this case, would be difficult to be detected in that scenario. As observed in Figures 2 and 3, the $P_{99\%}(\Delta\theta)$ can reach as high as 8° to 14° when using commercial transceivers, although being strongly reduced to around 2° when filtering is applied. As a result, the mechanical vibrations considered in this study would be obscured by noise in most cases (at different ROPs, OSNRs and N_{win}). The inset of Fig. 7(b) shows the high-pass filtered (HPF) time evolution of the Stokes vector when a vibration with f_{osc} = 26 and amplitude 10 V_{pp} is applied. The HPF with a 3 Hz cut-off frequency is used to enhance visualization, eliminating the DC component and preserving the mechanical ones. Depending on the specific fiber displacement, geometrical deformations, and induced stresses, S_3 oscillates more weakly compared to the other Stokes parameters. Consequently, relying on a single Stokes parameter for event detection could be misleading, potentially resulting in a misinterpretation of the overall picture.

Regarding the frequency components, Fig. 7(c) shows the PSDs for various induced vibrations on the fiber. Similarly to the spectrograms in Figures 5(b-d) and 6, these PSDs have been obtained by summing up the single PSDs of the three Stokes parameters. The 26 Hz event generates the strongest component, which attenuates as the vibration amplitude is reduced from 10 V_{pp} (blue curve) to 6 (orange curve) and 3 V_{pp} (yellow curve), while the other two components at 6 Hz and 40 Hz (green and light blue curves) are of comparable intensity. This picture provides valuable insights for the detection algorithms that will be discussed later, demonstrating that frequency content can be extremely useful for event detection.

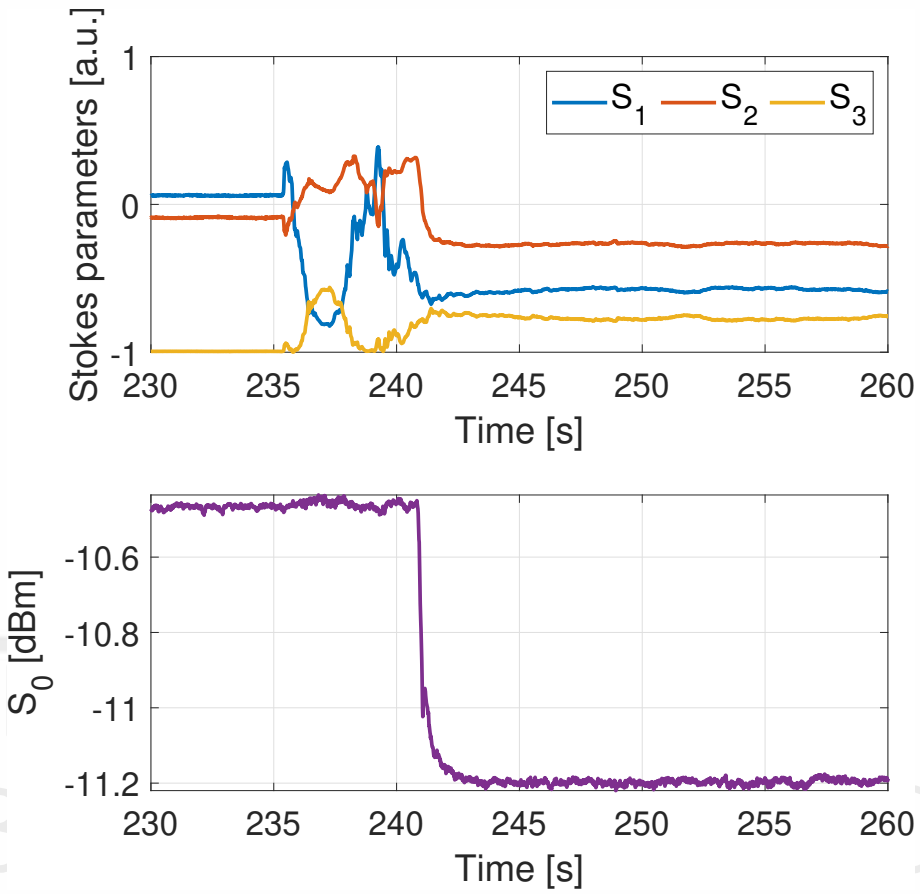

Fig. 9. Effect of hacker-like fiber spoofing on the Stokes parameters and on the instantaneous power S_0

4.2. Fiber spoofing

A malicious person, a hacker, could act on the telecommunication system's physical layer to eavesdrop on sensitive data and cause damage to the vendors. Among the different fiber-tampering techniques that have been identified [47], the most common one is fiber spoofing, which consists in macro-bending the fiber cable at a low curvature radius so that the total internal reflection condition allowing for light propagation is compromised and, in the bending point, light leaks from the fiber and can thus be captured by an eavesdropping device. One of the consequences for the communication system is a small received power drop [48,49], in parallel with a bending-induced SOP variation [50], both of which can be detected by a SOP-sensing system.

In order to emulate this kind of event, we employed a commercial optical fiber identifier (OFI) tool which, as shown in Fig. 4 in the dashed-blue block, clamps the laboratory fiber (in orange in Fig. 4), connected to the 35 km metropolitan ring (in green in Fig. 4), and heavily bends it [51]. The clamping is controlled by a handgrip, which is tightened to bend the fiber inside the instrument. When the device detects light leakage, a fiber spoofing event is generated.

To characterize the signature that the macro-bends have on the SOP, initial experiments were carried out with OFI firmly secured to the optical bench, isolating it from external agents. The fiber was gently clamped for 30 seconds and then released. The polarimeter outputs the complete Stokes vector, with the S_0 component recording instantaneous power. The results of ten tests are

shown in Fig. 8(a). The closing/opening of the clamp (around 7 and 37 seconds, respectively) cause the instantaneous power to transition gradually between levels over approximately one second. When the clamp is instead completely closed and pressing on the fiber, S_0 remains constant. To gain a more comprehensive understanding of S_0's response, the fiber spoofing tests were repeated about 120 times, revealing an average power drop of 0.3 dB.

Fig. 8(b) reports the behavior of the three Stokes parameters for the same ten tests, showing a strong impact of the macro-bends on the SOP. To quantify the impact of macro-bends on the polarization state [33], we computed the angular deviation as described in Fig. 1(c). Here the reference Stokes vector $\vec{S}_{ref}$ is the average Stokes vector measured a few seconds before the fiber spoofing, while $\vec{S}[n]$ represents the time evolution of the Stokes vector when the clamp is closed. For the 120 measured events, the average angular deviation $\Delta\theta$ was found to be 9°, which is three times greater than the deviation caused by the most intense vibration discussed in the previous subsection (see Fig. 7(a-b)).

In a real-life scenario, a malicious individual would likely manipulate the fiber before inserting it into the device, rather than keeping it completely firm over a surface. Additionally, the device would probably remain closed on the cable for several hours to intercept as much data as possible, rather than just for a few seconds. This more realistic hacking situation is depicted in Fig. 9. In this case, beyond the SOP angular deviation caused by clamping, the manipulation of the fiber before bending it is also considered. The Stokes parameters in Fig. 9 show abrupt changes just before the S_0 parameter drops, starting from second 235, when the fiber is handled to be inserted in the OFI. The power drop itself occurs at the 241st second, when the macro-bend is introduced. It is noteworthy that S_0 remains completely unaffected by any manipulation prior to clamping, as no power leakage is generated. The same applies to the induced vibrations discussed in Section 4.4.1. Given these characteristics of fiber spoofing, a possible detection algorithm could jointly monitor the Stokes vector and instantaneous power, triggering alerts only when both metrics exhibit significant changes. This approach would help differentiate malicious activities from generic power fluctuations or SOP variations caused by accidental, non-hazardous touches to the fiber.

4.3. Lightning strikes

Lightning strikes occurring near underground fiber cables or hitting aerial fibers can induce extremely rapid (krad/s to Mrad/s) polarization rotations due to the Faraday effect [52]. This can cause a loss of polarization tracking and potentially disrupt communications [40]. Although these events significantly impact the SOP, their duration is very brief, ranging from about 20 to 60 μs, as discussed in [53]. Therefore, lightning strikes are impossible to characterize and, most importantly, detect at the sampling rate discussed until now in this work. One potential solution for detecting such events could be to process the data stream directly from the coherent receiver equalizer without any decimation, targeting an SOP sampling frequency in the tens of MS/s range. However, managing the vast amount of data generated in this manner would be extremely complex and requires further careful consideration. Since this detection scenario is completely different from slow mechanical events, lightning strike occurrences will not be discussed further in this work.

5. SOP-based Algorithms for automatic detection of anomalous events

The scenarios and events discussed in the previous Section have highlighted various types of perturbations affecting the state of polarization. This suggests that by analyzing the time evolution of the SOP, it is possible to detect harmful and anomalous events occurring along the deployed optical fiber path.

In this Section, we describe two DSP algorithms that we proposed in our previous works [21, 22, 41, 42]. The first method evaluates the SOP angular speed (SOPAS, see Subsection

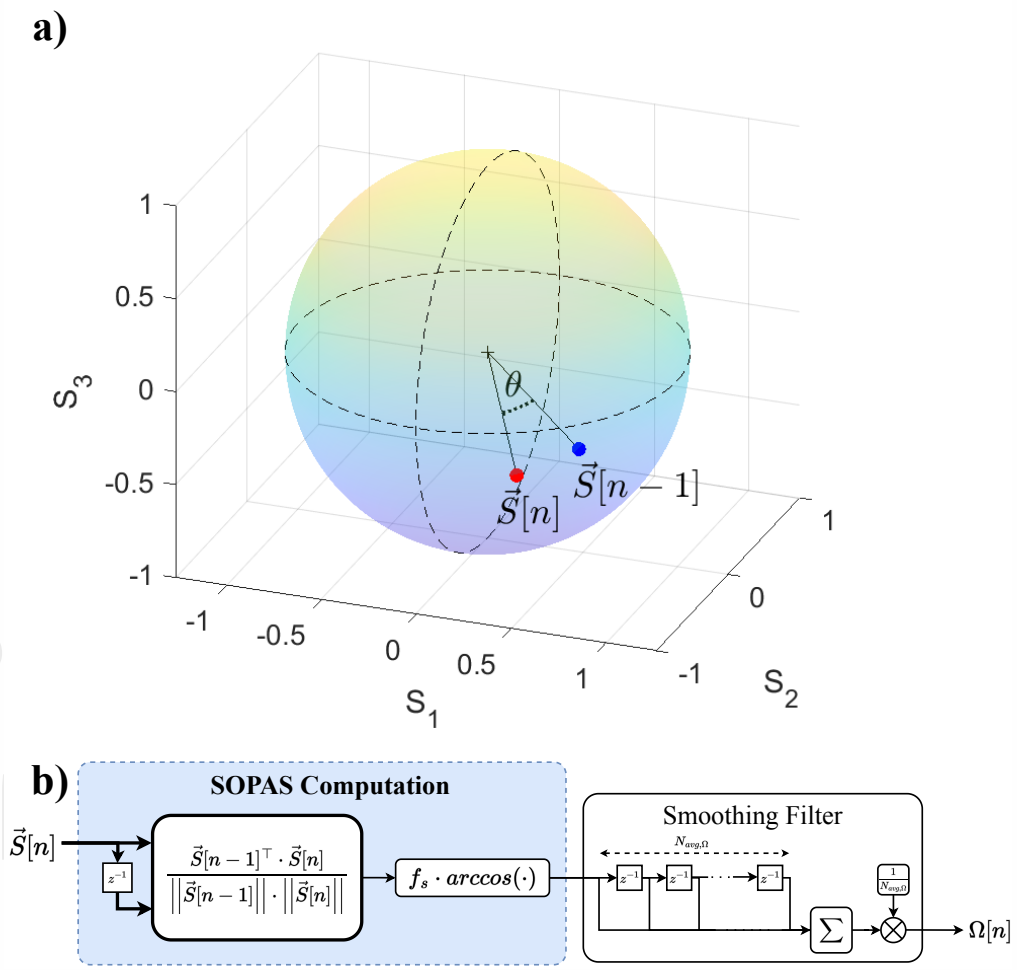

Fig. 10. (a) Poincaré sphere where an example of two consecutive Stokes vectors (blue dot $\vec{S}[n-1]$, red dot $\vec{S}[n]$), and the angle θ in between them has been reported, to make the scheme in (b) more clear. (b) DSP scheme for the SOPAS anomaly detection algorithm, where $\Omega[n]$ is the SOPAS post-smoothing filter. $\vec{S}[n]$ is the input Stokes vector time series.

5.5.1) using a simple, non-adaptive, time-domain solution. The second method (SOP-PSDG, see Subsection 5.5.2) employs a more advanced, frequency-based scheme capable of adaptively tracking the non-stationarity of the SOP fluctuations that typically occur in the deployed optical fiber scenario. Both methods detect anomalous events by raising an alarm when a processed signal, derived from the SOP evolution, exceeds a given threshold.

5.1. Time-based solution: the SOPAS algorithm

A straightforward method for detecting anomalies using a threshold-based approach involves monitoring the rate at which the SOP varies over time. This can be achieved by evaluating its angular speed, i.e. measuring the variation over time of the angle between two consecutive Stokes vectors over the Poincaré sphere (illustrated as θ in Figure 10(a)). The SOPAS signal $\Omega[n]$ can

be computed from the Stokes vector $\vec{S}[n]$, according to (3):

$$\Omega[n] = f_s \cdot \arccos\left(\frac{\vec{S}[n-1]^\top \cdot \vec{S}[n]}{||\vec{S}[n-1]|| \cdot ||\vec{S}[n]||}\right). \tag{3}$$

Figure 10(b) illustrates the DSP scheme used to compute the SOPAS. The scheme includes also a smoothing filter, implemented as a moving average, to attenuate the SOPAS fluctuations caused by the SOP environmental noise, discussed in previous sections.

This metric requires only the current and previous SOP samples, making it extremely simple to compute, even in real-time scenarios. However, it is not adaptive to slow daily urban changes of the SOP, as they require more consecutive SOP samples in order to be effectively monitored. This characteristic makes it suitable for scenarios where anomalous conditions are well-defined and cause polarization rotations significantly faster than those generated by the surrounding environment.

Additionally, the SOPAS has an upper limit bounded by the employed sampling frequency f_s, since the arc length drawn over the Poincaré sphere surface cannot exceed π without resulting in undersampling, as stated in [53]. This means that the maximum measurable SOPAS is given by the relationship $\Omega_{max} = \pi \cdot f_s$ [rad/s], which is anyway usually sufficient if considering mechanical vibrations and stresses.

5.2. Adaptive and spectrally-resolved solution: the SOP-PSDG algorithm

When environmental agents surrounding the fiber induce polarization rotations at speeds comparable to those caused by anomalous events, the SOPAS algorithm may become ineffective. However, as observed in the SOP spectrograms in Section 3, SOP environmental noise contributes to the spectrum at specific (though not static) frequencies, which can significantly differ from the frequencies excited during an anomalous event. Consequently, an alternative approach to process the SOP evolution for anomaly detection can be to compute a metric based on the analysis of the evolution of Stokes parameters in the frequency domain, i.e. studying how the SOP PSD changes over time.

The method we propose, simple yet effective, involves comparing historical values of the SOP PSD (i.e., the time-domain average of the SOP PSD spectrogram) with current SOP PSD values computed in real-time from the Stokes vector time series. The main idea is that anomalies are likely to occur when the current SOP PSD deviates significantly from its historical average. This concept is illustrated in the spectrogram in Figure 11, where a mechanical vibration is induced by a shaker on the experimental setup (with an oscillation frequency of $f_{osc} = 40$ Hz). By examining the spectrogram, the anomalous event can be easily identified by simply comparing the time-domain average PSD of the SOP in a quiescent condition (e.g., the area within the solid violet rectangle in Figure 11) against the PSD computed when the anomaly affects the SOP (dashed violet line in Figure 11). By quantifying this discrepancy, unexpected PSD patterns can be identified as anomalies, leading us to the design of the SOP-Power Spectral Density Gap (SOP-PSDG) algorithm.

The DSP scheme for SOP-PSDG-based anomaly detection is illustrated in Figure 12. The proposed algorithm extends the DSP scheme we proposed in [42], including implementation details on its real-time adaptive capabilities. The real-time SOP-PSDG is calculated as follows. First, each of the three $\vec{S}[n]$ components (where n represents the discrete-time index), $S_1[n]$, $S_2[n]$ and $S_3[n]$, is stored into a tapped delay line of N_{FFT} consecutive samples, from which, at each sampling time a one-sided PSD is evaluated: its computation is implemented by means of real-valued Fast Fourier Transform (FFT) [54], followed by the computation of the square magnitude of the FFT points. The evolution of the PSDs of the three Stokes parameters is

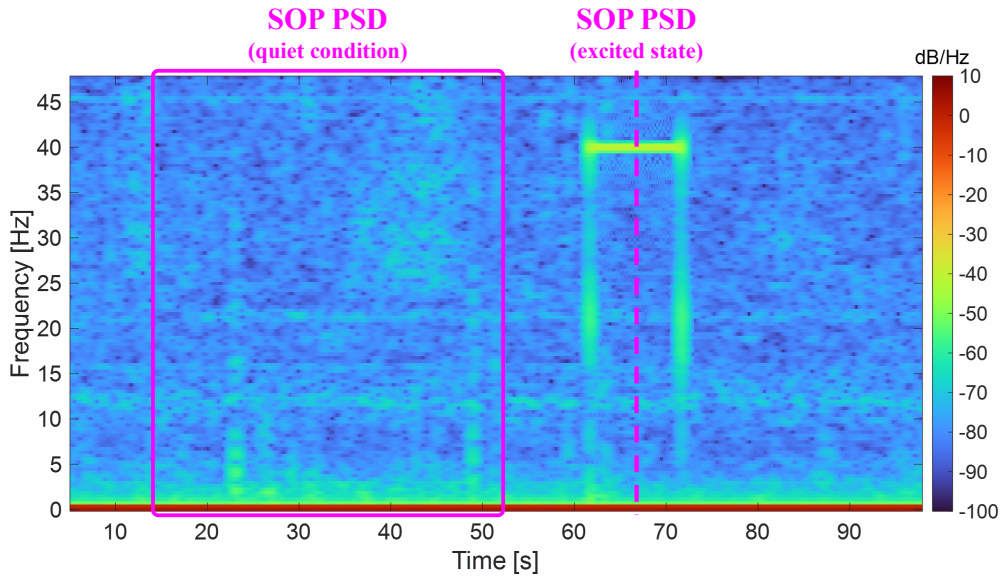

Fig. 11. SOP spectrogram, computed as the sum of the three Stokes parameters PSDs, acquired over the 35 km metropolitan fiber when inducing a mechanical vibration (f_{osc} = 40 Hz) for 10 seconds. The area within the solid violet rectangle is the SOP PSD in a quiescent condition, while the dashed violet line is the SOP PSD when the anomaly affects the fiber.

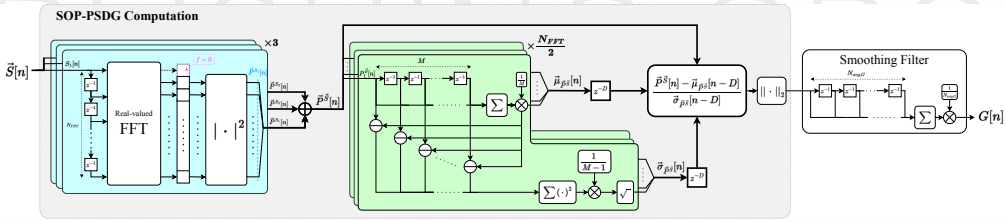

Fig. 12. DSP scheme for the SOP-PSDG anomaly detection algorithm. Light-blue DSP blocks indicate operations on individual Stokes vector parameters, while light-green DSP blocks denote operations on individual SOP PSD frequency components. Thick lines represent element-wise operations on vector signals.

represented by the signal vectors $\vec{P}^{S_1}[n]$, $\vec{P}^{S_2}[n]$ and $\vec{P}^{S_3}[n]$, defined as follows:

$$\vec{P}^{S_i}[n] = \left[P_1^{S_i}[n], P_2^{S_i}[n], \ldots, P_{\frac{N_{FFT}}{2}}^{S_i}[n] \right], \qquad i = 1, 2, 3 \tag{4}$$

where $P_k^{S_i}[n]$ represents the value of the k-th PSD point at the time index n relative to the i-th Stokes parameter. For practical reasons, in the computed PSDs, we discard the FFT point relative to the lowest frequency bin ($f = 0$), as shown in Fig.12. This removal helps exclude discrepancies relative to the "stationary" SOP (i.e., the average value of the Stokes Parameters) from the metric computation, as they are not relevant for anomaly detection purposes. The stationary SOP can indeed slowly vary over time, encompassing the entire Poincaré sphere even in the absence of anomalies.

The three computed PSDs are then summed together element-wise, to form the vector

$\vec{P}^{\vec{S}}[n] = \vec{P}^{S_1}[n] + \vec{P}^{S_2}[n] + \vec{P}^{S_3}[n]$ (as done in Section 3 when analyzing the SOP spectra). This single SOP PSD constitutes an "isotropic" representation of the SOP power spectral content: indeed, $\vec{P}^{\vec{S}}[n]$ provides information on the fluctuations of the SOP over the Poincaré sphere regardless of the direction of these variations.

Finally, the SOP-PSDG signal $G[n]$ is obtained as the Euclidean norm of the difference between the current SOP-PSD vector $\vec{P}^{\vec{S}}[n]$ and its moving average $\vec{\mu}_{\vec{P}^{\vec{S}}}[n] = \left[\mu_{P_1^{\vec{S}}}[n], \mu_{P_2^{\vec{S}}}[n], \dots\right]$ delayed by D sample-times (referred to as *margin delay*), as follows:

$$G[n] = \sqrt{\sum_{k=1}^{\frac{N_{FFT}}{2}} \frac{1}{\sigma_{P_k^{\vec{S}}}[n-D]^2} \left(P_k^{\vec{S}}[n] - \mu_{\vec{P}_k^{\vec{S}}}[n-D]\right)^2}, \tag{5}$$

where $\vec{\sigma}_{\vec{P}^{\vec{S}}}[n] = \left[\sigma_{P_1^{\vec{S}}}[n], \sigma_{P_2^{\vec{S}}}[n], \dots\right]$ represent the moving standard deviation of the elements in $\vec{P}^{\vec{S}}[n]$. As done for the SOPAS, the SOP-PSDG scheme also incorporates a smoothing filter applied to attenuate the $G[n]$ fluctuations. In (5), the normalization of both the current and average SOP-PSD values with respect to their standard deviation allows the algorithm to account for variability in the intensity of the frequency components in the SOP spectrum. In this way, frequency components with more unstable or variable intensities are appropriately weighted, preventing random increases in $G[n]$ values under normal conditions (and thereby enhancing anomaly detection performance).

As shown in Figure 12, the moving averages and standard deviations of the spectral elements of the SOP PSD are continuously computed over $N_{FFT}/2$ separated tapped delay lines, each with a *memory* of M consecutive samples. This approach provides a DSP scheme with adaptive capability, able to memorize and track the pattern and variability of the SOP PSD in real-time. Consequently, the algorithm can adapt to the non-stationary behavior of the SOP PSD, which varies on an hourly basis (as observed in Section 3).

Moreover, as illustrated in Figure 12 and (5), both $\vec{\mu}_{\vec{P}^{\vec{S}}}$ and $\vec{\sigma}_{\vec{P}^{\vec{S}}}$ are delayed by D samples with respect to the current SOP PSD $\vec{P}^{\vec{S}}[n]$: this ensures that anomalies are not memorized by the DSP-scheme immediately upon their occurrence, which would degrade the detection capability of the algorithm. In fact, a margin delay $D > N_{FFT}$ is sufficient to prevent this issue, since in this way $D - N_{FFT}$ samples are required to be processed before the SOP-PSDG scheme starts to adapt its statistics to the anomaly.

Compared to SOPAS, this metric is clearly more complex, requiring the storage of more SOP samples and the accumulation of statistics on the SOP spectrum. Nevertheless, its ability to adapt to slow variations in the SOP provides a significant advantage in detecting anomalous events, as we will illustrate in the next section.

6. Experimental results using SOP-based algorithms.

The two DSP schemes illustrated in the previous section will now be evaluated based on their responses to the anomalous events described in Section 4. To ensure a fair comparison of the two methods in terms of detection delay induced by the DSP scheme, the smoothing filter length employed to compute the SOPAS has been set to $N_{avg,\Omega} = 287$ samples (corresponding to 3 seconds with f_s=95.4 Hz) [42]. For the SOP-PSDG, the smoothing filter length is adjusted to $N_{avg,G} = N_{avg,\Omega} - N_{FFT}$ samples, to account for the delay induced by FFT input tapped delay line (see Figures 10 and 12). Unless stated otherwise, all subsequent results will use these parameters with $N_{FFT} = 128$ points.

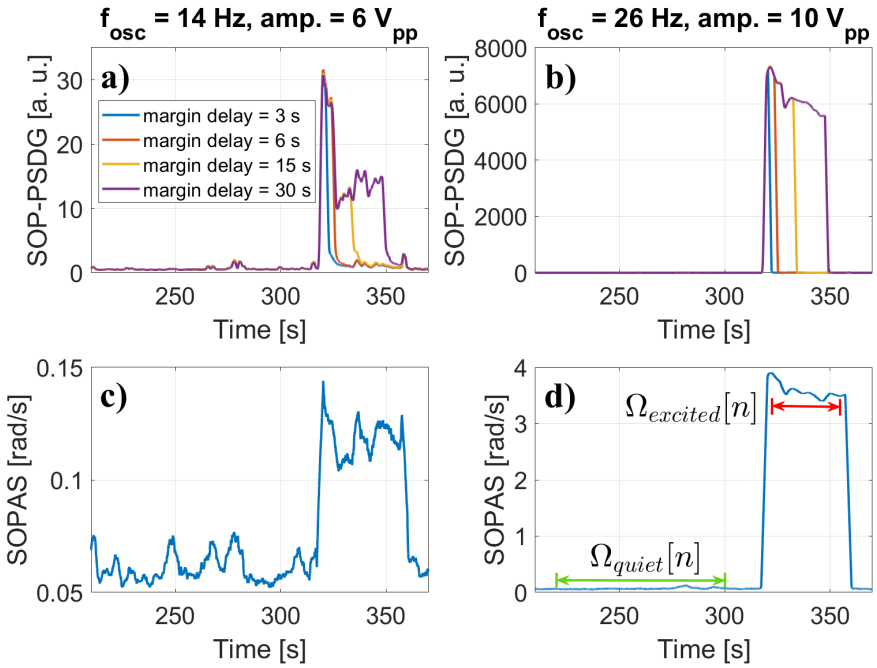

Fig. 13. (a-b) SOP-PSDG signal when f_{osc} = 14 Hz, amp. = 6 V_{pp} and f_{osc} = 26 Hz, amp. = 10 V_{pp}, for different values of margin delay. Legend in (a) applies also to (b). (c-d) SOPAS signal when f_{osc} = 14 Hz, amp. = 6 V_{pp} and f_{osc} = 26 Hz, amp. = 10 V_{pp}.

6.1. Mechanical vibrations detection using SOPAS and SOP-PSDG

Figure 13 illustrates the evolutions of the SOP-PSDG and SOPAS under two different vibration scenarios induced by a mechanical shaker in the experimental setup described in Fig. 4), considering the 35 km long fiber. In the first scenario, the setup was configured to produce an angular deviation of approximately 1° (see Figure 7(a)), with an oscillation frequency of 14 Hz and a peak-to-peak voltage of 6 V_{pp} (Figures 13(a) and (c)). The second scenario, characterized by a more intense vibration, induced an angular deviation of approximately 3°, with an oscillation frequency of 26 Hz and a peak-to-peak voltage of 10 V_{pp} (Figures 13(b) and (d)). For this analysis, the memory duration was set to 180 seconds (i.e. M around $17 \cdot 10^3$ samples), while various margin delays were tested, ranging from 3 to 30 seconds.

In Figure 13, both the SOPAS and SOP-PSDG methods detect anomalies at approximately 320 seconds for the induced vibrations. However, the SOP-PSDG signal demonstrates a key advantage: after the specified margin delay has been surpassed, it quickly returns to its pre-detection levels. This indicates that the SOP-PSDG can rapidly adapt to changing conditions once the margin delay has been exceeded. Furthermore, comparing Figures 13(a) and (c) reveals that, during detection, the SOP-PSDG signal shows a significantly larger relative increase (up to one order of magnitude) compared to the SOPAS, which only shows a doubling of its pre-detection values. This difference highlights the superior sensitivity of the frequency-based SOP-PSDG algorithm.

In order to quantitatively compare the sensitivity of the two algorithms, we define a detection Signal-to-Noise Ratio (SNR) as the ratio between the average squared values of the detection signal in excited and quiet conditions. For instance, the SNR of the SOPAS signal is defined as

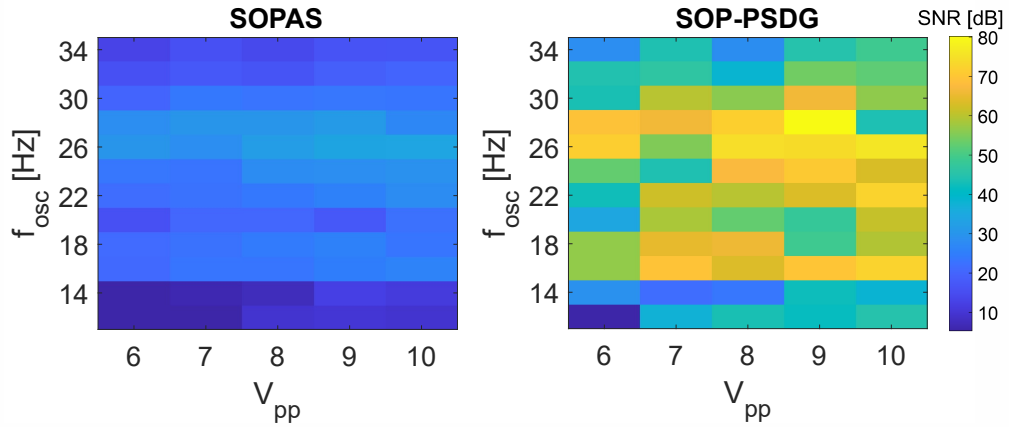

Fig. 14. SNRs computed for SOPAS and SOP-PSDG at different f_{osc} and V_{pp}.

follows:

$$SNR_{SOPAS} = \frac{\mathbb{E}\left[\left(\Omega_{excited}[n]\right)^2\right]}{\mathbb{E}\left[\left(\Omega_{quiet}[n]\right)^2\right]}. \tag{6}$$

As shown in Fig. 13(c), $\Omega_{quiet}[n]$ refers to a few tens of seconds before the vibration is activated. $\Omega_{excited}[n]$ refers instead to the samples related to the event acting on the fiber, neglecting the transients due to the smoothing filter. The same windowing of Fig. 13(c) and (6) has been applied on the SOP-PSDG, considering $G_{quiet}[n]$ and $G_{excited}[n]$. The latter refers to the SOP-PSDG samples when the vibration is activated, up to the margin delay value, neglecting the transients due to the smoothing filter and FFT. Figure 14 displays the evolution of the detection SNR over a subset of the cases considered in Section 4.4.1 (refer to Fig. 7(a)). For this analysis, the SOP-PSDG margin delay was set to 10 seconds. For all the combinations of f_{osc} and V_{pp}, the SOP-PSDG exhibits a consistently higher SNR (50 dB-70 dB) than the SOPAS (20 dB-40 dB).

6.2. Fiber-spoofing detection using SOPAS and SOP-PSDG

As outlined in Subsection 4.4.2, fiber spoofing events have been simulated through an OFI over the 35 km long fiber. Each spoofing event was replicated 100 times, with each occurrence lasting 30 seconds and separated by 60 seconds. The relevant phase of each event was the closing of the fiber insertion clamp, rather than its release. This means that spoofing detection needs to occur promptly after the clamp starts closing.

Figure 15 illustrates the responses of the SOP-PSDG and SOPAS to several fiber spoofing events. For the SOP-PSDG algorithm, the memory M has been set to 30 seconds (i.e. M around $2.8 \cdot 10^3$ samples), while the margin delay has been fixed at 5 seconds. The insertion of the fiber into the clamp causes a noticeable increase in both SOPAS and SOP-PSDG signals, occurring about 7-8 seconds before the S_0 drop. This early rise highlights the superior responsiveness of the SOP-based DSP schemes, which is crucial for minimizing the data leakage during a fiber spoofing attack. Notably, the SOP-PSDG signal drops after 5 seconds, coherently with the imposed margin delay, while the SOPAS signal remains in its excited state until the fiber stabilizes within the OFI device.

6.3. SOPAS and SOP-PSDG methods on SOP data from a coherent receiver

As a final discussion, we present preliminary results using both methods on SOP data collected from the commercial coherent transceiver described in Section 2, which replaces the laser

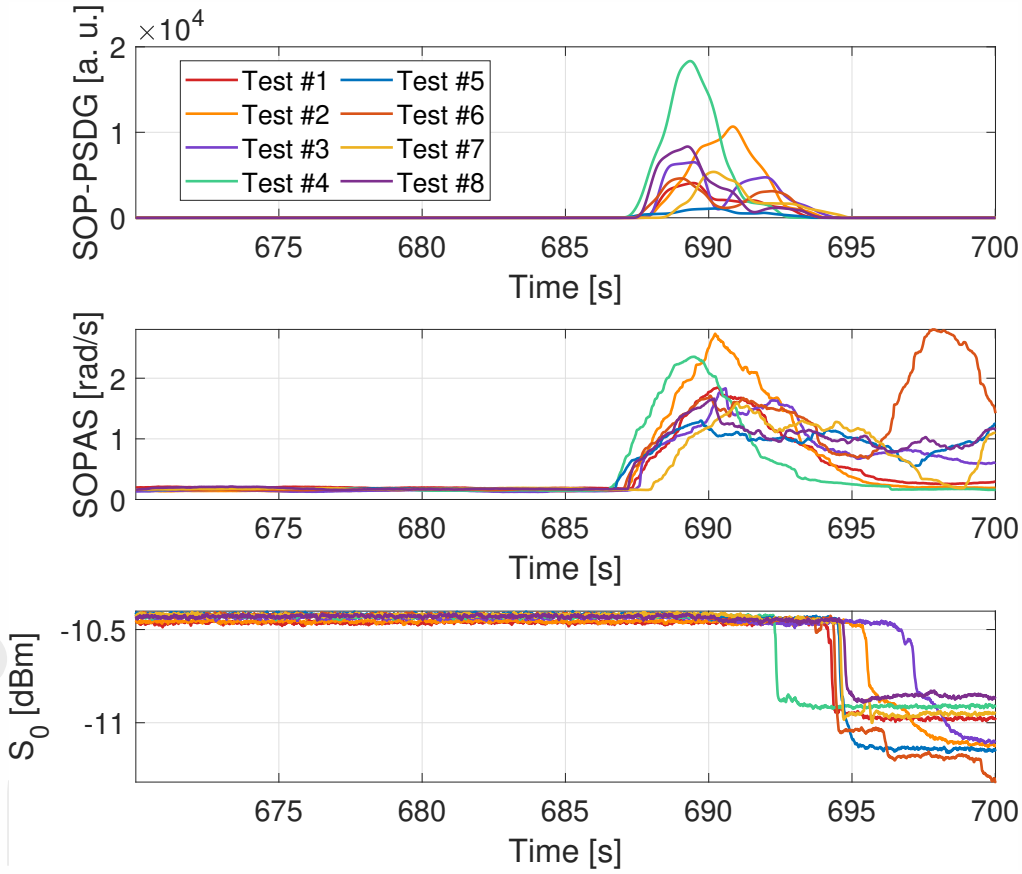

Fig. 15. Hacker-like spoofing effect on SOP-PSDG, SOPAS and S_0.

and polarimeter depicted in Fig. 4. For this experiment, to further change the scenario and demonstrate how the two algorithms work and compare in a completely different condition, we exploited the 10 km long metropolitan fiber (indicated red line in Fig. 4). Given the significant SOP estimation noise in this scenario, as detailed in Section 2 (see Fig. 3), we introduced strong mechanical vibrations using a mechanical shaker. For this purpose, the vibrating plate has been substituted with a circular metallic one, which is most intense on the fiber for an oscillation frequency of 20 Hz and a peak-to-peak voltage of 10 V_{pp}. The $P_{99\%}(\Delta\theta)$ is around 2° in the absence of vibration and increases to 4° when vibrations are applied. 130 vibrational events lasting 5 seconds each have been periodically induced in the experimental setup. Fig. 16 shows the corresponding SOP-PSDG and SOPAS evolutions for each event. The SOPAS scheme used a smoothing filter with $N_{avg,\Omega} = 76$ samples (corresponding to approximately 4 seconds) and sampled at $f_s = 19$ S/s. To achieve a similar detection delay with the SOP-PSDG, N_{FFT} was set to 64 points and $N_{avg,G}$ to 12. The SOP-PSDG memory was set to 180 seconds, with a margin delay of 3 seconds. As shown in Fig. 16, the SOP-PSDG seems to effectively react to the induced anomaly events: during detection, the PSDG values increase by around one order of magnitude compared to pre-detection levels. In contrast, due to the smoothing filter, the SOPAS signal stays high and nearly constant before detection, with peak intensities only doubling when an event occurs. In summary, preliminary results indicate that SOP-PSDG outperforms SOPAS for threshold-based detection even when using commercial coherent receivers.

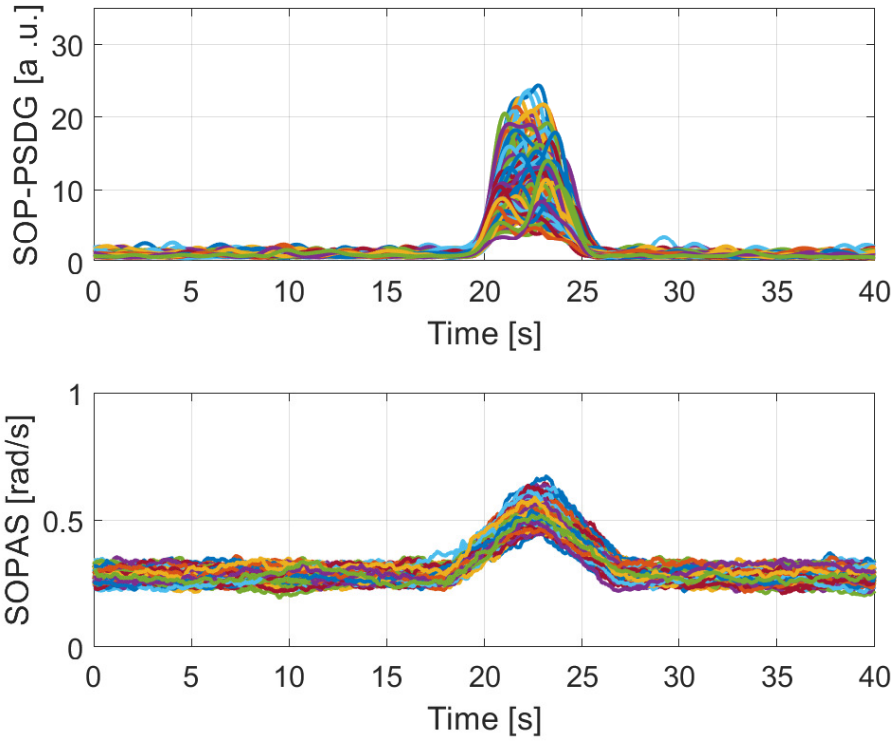

Fig. 16. Several occurrences of SOP-PSDG and SOPAS signals considering SOP data extracted from the commercial transceiver, when a vibration having f_{osc} = 20 Hz and amplitude 10 V_{pp} is induced on the fiber.

7. Discussions and Conclusions

In this work, we analyzed polarization sensing in an urban environment, employing metropolitan fibers running around Turin, in Italy. We first characterized the accuracy of the SOP data provided by a commercial coherent transceiver (able to output the SOP samples at around 20 S/s), evaluating the estimation noise cloud spread over the Poincaré sphere surface. The results obtained in both an ASE noise-limited scenario and ROP-limited one underline the possibility of enhancing the accuracy, which was originally quite low. $P_{99\%}(\Delta\theta)$ values can reach 8° to 14° in the worst cases. Using a simple low-pass filter improves accuracy even by a factor of four, using a window length of $N_{\text{win}} = 15$ samples (see Figures 2 and 3). The matching between experimental and numerical simulation results also suggests that the SOP data stream, sampled at sampling frequencies of the order of the symbol rate, could be low-passed and then decimated, keeping the SOP estimate accuracy fixed. Due to the low-frequency components generated by mechanical vibrations, a sampling frequency of around a few tens of Hz could also be suitable to reduce processing and data storage complexity.

A characterization of the SOP fluctuations generated by the urban scenario, which we called SOP environmental noise, has been provided, showing different agents that could impinge on the cable and enhance the noise. Experiments have been carried out exploiting a polarimeter so that the sampling frequency could be tweaked for our purposes, and set to 95.4 S/s. Specifically, time-varying external conditions to which the fiber is subject generate SOP fluctuations, making

it non-stationary. This represents an issue for any anomaly detection algorithms. On top of this scenario, we have shown the effect of different mechanical vibrations on the SOP, characterizing the effect that they have on the cloud of points on the surface of the Poincaré sphere, as Stokes vector time evolution and frequency content. This analysis showed that different vibrations have particularly strong or weak effects on the fiber cable, which translates to SOP angular deviation. Fiber spoofing has also been characterized, showing a strong effect on the SOP variation and instantaneous power drop.

Two different algorithms have then been proposed to process the data and allow for anomaly detection, based on threshold application. The SOPAS method is time-resolved and non-adaptive, whereas the SOP-PSDG is frequency-resolved and adaptive. Especially for the SOPAS algorithm, baseline noise characterization is fundamental in understanding which anomalies can be revealed. The surrounding environment may present different SOP noise levels depending on non-harmful external agents acting on the fiber. Due to its ability to adapt to changing conditions, the SOP-PSDG method is more suitable for use in environments such as metropolitan areas, where it demonstrated enhanced sensitivity compared to the SOPAS method under all tested conditions. Both the SOP-PSDG and SOPAS methods can be combined with a threshold on the instantaneous power to detect fiber spoofing. However, once the memory and margin delay are set, the SOP-PSDG method appears to outperform the SOPAS approach. Results employing a commercial coherent transceiver connected to a metropolitan fiber have also been shown. The two methods have been compared when a vibration is induced on the fiber. Despite the disadvantageous conditions due to the low sampling frequency and very high SOP estimation noise, SOP-PSDG demonstrated to outperform the SOPAS method even in this condition.

The latest research on anomaly detection of hazardous conditions within the optical network's physical layer broadly employs machine learning techniques [55–57], particularly for fiber spoofing events, earthquakes [6, 58], but also for traffic monitoring [59]. Nevertheless, a DSP algorithm that can output a signal indicating an anomalous condition without requiring prior training could be extremely useful. When used in conjunction with neural networks, this approach could enable much more reliable detection of potentially hazardous events. Key features such as event duration and signature over the Poincaré sphere surface could be used as further detection parameters. This would enhance the resilience of optical networks to fiber cuts in metropolitan environments, robustness against eavesdropping, and potentially offer early warnings for a wide range of anomalous conditions not only limited to the urban scenario.

8. Acknowledgments

Saverio Pellegrini, Giuseppe Rizzelli and Roberto Gaudino are also sponsored by the SURENET project – funded by European Union – Next Generation EU within the PRIN 2022 program (D.D. 104 - 02/02/2022 Ministero dell'Università e della Ricerca). This manuscript reflects only the authors' views and opinions and the Ministry cannot be considered responsible for them.
The authors wish to express their gratitude to Novoptel GmbH, who co-authored the OFC2024 paper [41] from which this Journal article is derived. Novoptel GmbH played a pivotal role in facilitating the demo session at OFC2024, by providing the necessary hardware (polarimeter PM1000 and laser LU1000) and offering technical support.

References

1. L. Schenato, "A Review of Distributed Fibre Optic Sensors for Geo-Hydrological Applications," Appl. Sci. **7** (2017).
2. L. Schenato, A. Pasuto, A. Galtarossa, and L. Palmieri, "On the use of OFDR for high-spatial resolution strain measurements in mechanical and geotechnical engineering," in *Proceedings of the 2018 IEEE International Instrumentation and Measurement Technology Conference (I2MTC),* (2018), pp. 1–6.
3. N. J. Lindsey, S. Yuan, A. Lellouch, *et al.*, "City-Scale Dark Fiber DAS Measurements of Infrastructure Use During the COVID-19 Pandemic," Geophys. Res. Lett. **47** (2020).

4. J. Liu, S. Yuan, Y. Dong, *et al.*, "TelecomTM: A Fine-Grained and Ubiquitous Traffic Monitoring System Using Pre-Existing Telecommunication Fiber-Optic Cables as Sensors," Proc. ACM Interact. Mob. Wearable Ubiquitous Technol. **7** (2023).
5. A. Fichtner, A. Bogris, T. Nikas, *et al.*, "Theory of phase transmission fibre-optic deformation sensing," Geophys. J. Int. **231**, 1031–1039 (2022).
6. W. Zhu, E. Biondi, J. Li, *et al.*, "Seismic arrival-time picking on distributed acoustic sensing data using semi-supervised learning," Nat. Commun. **14** (2023).
7. E. F. Williams, M. R. Fernández-Ruiz, R. Magalhaes, *et al.*, "Distributed sensing of microseisms and teleseisms with submarine dark fibers," Nat. Commun. **14** (2019).
8. M.-F. Huang, M. Salemi, Y. Chen, *et al.*, "First Field Trial of Distributed Fiber Optical Sensing and High-Speed Communication Over an Operational Telecom Network," J. Light. Technol. **38**, 75–81 (2020).
9. E. Ip, Y.-K. Huang, M.-F. Huang, *et al.*, "DAS Over 1,007-km Hybrid Link With 10-Tb/s DP-16QAM Co-Propagation Using Frequency-Diverse Chirped Pulses," J. Light. Technol. **41**, 1077–1086 (2023).
10. Y. Muanenda, C. J. Oton, S. Faralli, and F. Di Pasquale, "A Cost-Effective Distributed Acoustic Sensor Using a Commercial Off-the-Shelf DFB Laser and Direct Detection Phase-OTDR," IEEE Photonics J. **8**, 1–10 (2016).
11. Y. Koyamada, M. Imahama, K. Kubota, and K. Hogari, "Fiber-Optic Distributed Strain and Temperature Sensing With Very High Measurand Resolution Over Long Range Using Coherent OTDR," J. Light. Technol. **27**, 1142–1146 (2009).
12. L. Andrenacci, D. Pilori, S. Pellegrini, *et al.*, "Comparison between Phase and Polarization Sensing using Coherent Transceivers over Deployed Metro Fibers," in *Optical Fiber Communication Conference (OFC) 2024,* (Optica Publishing Group, 2024), p. M2K.2.
13. G. Marra, D. M. Fairweather, V. Kamalov, *et al.*, "Optical interferometry–based array of seafloor environmental sensors using a transoceanic submarine cable," Science **376**, 874–879 (2022).
14. S. Donadello, C. Clivati, A. Govoni, *et al.*, "Seismic monitoring using the telecom fiber network," Commun. Earth & Environ. **5** (2024).
15. A. Bogris, T. Nikas, C. Simos, *et al.*, "Sensitive seismic sensors based on microwave frequency fiber interferometry in commercially deployed cables," Sci. Reports **12** (2022).
16. I. Di Luch, P. Boffi, M. Ferrario, *et al.*, "Vibration Sensing for Deployed Metropolitan Fiber Infrastructure," J. Light. Technol. **39**, 1204–1211 (2021).
17. I. Di Luch, M. Ferrario, G. Rizzelli, *et al.*, "Vibration Sensing for Deployed Metropolitan Fiber Infrastructures," in *Proceedings of 2020 Optical Fiber Communications Conference and Exhibition,* (2020).
18. I. Di Luch, M. Ferrario, P. Boffi, *et al.*, "Demonstration of structural vibration sensing in a deployed PON infrastructure," in *Proceedings of the 45th European Conference on Optical Communication (ECOC 2019),* (2019), pp. 1–3.
19. G. Marra, C. Clivati, R. Luckett, *et al.*, "Ultrastable laser interferometry for earthquake detection with terrestrial and submarine cables," Science **361**, 486–490 (2018).
20. E. Ip, Y.-K. Huang, G. Wellbrock, *et al.*, "Vibration Detection and Localization Using Modified Digital Coherent Telecom Transponders," J. Light. Technol. **40**, 1472–1482 (2022).
21. S. Pellegrini, G. Rizzelli, M. Barla, and R. Gaudino, "Algorithm Optimization for Rockfalls Alarm System Based on Fiber Polarization Sensing," IEEE Photonics J. **15**, 1–9 (2023).
22. S. Pellegrini, G. Rizzelli, M. Barla, and R. Gaudino, "Polarization-Based Fiber Optic System for Debris Flow Early Warning: On-Field Demonstration," IEEE Photonics J. pp. 1–8 (2024).
23. C. J. Carver and X. Zhou, "Polarization sensing of network health and seismic activity over a live terrestrial fiber-optic cable," Commun. Eng. **3** (2024).
24. J. E. Simsarian and P. J. Winzer, "Shake Before Break: Per-Span Fiber Sensing with In-Line Polarization Monitoring," in *Optical Fiber Communication Conference,* (Optica Publishing Group, 2017), p. M2E.6.
25. P. Barcik and P. Munster, "Measurement of slow and fast polarization transients on a fiber-optic testbed," Opt. Express **28**, 15250–15257 (2020).
26. Z. Zhan, M. Cantono, V. Kamalov, *et al.*, "Optical polarization–based seismic and water wave sensing on transoceanic cables," Science **371**, 931–936 (2021).
27. K. S. Y. Skarvang, S. Bjørnstad, R. A. Rørstadbotnen, *et al.*, "Observation of local small magnitude earthquakes using state of polarization monitoring in a 250km passive arctic submarine communication cable," in *2023 Optical Fiber Communications Conference and Exhibition (OFC),* (2023), pp. 1–3.
28. K. S. Yamase Skarvang, S. Bjørnstad, E. Sæthre, and D. R. Hjelme, "Local Wind Impact Sensing using State of Polarization Measurement on a Live Short-Haul Aerial Fibre Cable," in *2024 Optical Fiber Communications Conference and Exhibition (OFC),* (2024), pp. 1–3.
29. R. Bratovich, F. M. R., S. Straullu, *et al.*, "Surveillance of Metropolitan Anthropic Activities by WDM 10G Optical Data Channels," in *2022 European Conference on Optical Communication (ECOC),* (2022), pp. 1–4.
30. J. Sakai and T. Kimura, "Birefringence and polarization characteristics of single-mode optical fibers under elastic deformations," IEEE J. Quantum Electron. **17**, 1041–1051 (1981).
31. E. Frins and W. Dultz, "Rotation of the polarization plane in optical fibers," J. Light. Technol. **15**, 144–147 (1997).
32. L. Palmieri and A. Galtarossa, "Coupling Effects Among Degenerate Modes in Multimode Optical Fibers," IEEE Photonics J. **6**, 1–8 (2014).
33. R. Ulrich and S. C. Rashleigh and W. Eickhoff, "Bending-induced birefringence in single-mode fibers," Opt. Lett. **5**,

273–275 (1980).
34. R. Ulrich and A. Simon, "Polarization optics of twisted single-mode fibers," Appl. Opt. **18**, 2241–2251 (1979).
35. K. Okamoto, *Fundamentals of Optical Waveguides* (Elsevier Science, 2006).
36. D. Goldstein, *Polarized Light* (CRC Press, 2017).
37. A. Mecozzi, M. Cantono, G. C. Castellanos, *et al.*, "Polarization sensing using submarine optical cables," Optica **8**, 788–795 (2021).
38. L. Costa, S. Varughese, P. Mertz, *et al.*, "Localization of seismic waves with submarine fiber optics using polarization-only measurements," Commun. Eng. **2** (2023).
39. A. Mecozzi, C. Antonelli, M. Mazur, *et al.*, "Use of Optical Coherent Detection for Environmental Sensing," J. Light. Technol. **41**, 3350–3357 (2023).
40. J. Tang, X. Li, C. Cheng, *et al.*, "Forward-transmission based distributed fiber sensing compatible with C+L unidirectional communication systems," in *2024 Optical Fiber Communications Conference and Exhibition (OFC),* (2024), pp. 1–3.
41. S. Pellegrini, L. Minelli, L. Andrenacci, *et al.*, "Real-Time Demonstration of Anomalous Vibrations Detection in a Metro-like Environment using a SOP-based Algorithm," in *2024 Optical Fiber Communications Conference and Exhibition (OFC),* (2024), pp. 1–3.
42. L. Minelli, S. Pellegrini, L. Andrenacci, *et al.*, "SOP-based DSP blind anomaly detection for sensing on deployed metropolitan fibers," in *49th European Conference on Optical Communications (ECOC 2023),* vol. 2023 (2023), pp. 519–522.
43. S. Pellegrini, L. Andrenacci, L. Minelli, *et al.*, "Estimation accuracy of polarization state from coherent receivers for sensing applications," in *2023 IEEE Photonics Conference (IPC),* (2023), pp. 1–2.
44. S. J. Savory, "Digital filters for coherent optical receivers," Opt. Express **16**, 804–817 (2008).
45. S. Benedetto and P. Poggiolini, "Polarization shift keying: an efficient coherent optical modulation," in *SBT/IEEE International Symposium on Telecommunications,* (1990), pp. 14–20.
46. M. A. Soto and J. A. Ramírez, "Earthquake monitoring using fibre-optic distributed acoustic sensing," in *49th European Conference on Optical Communications (ECOC 2023),* vol. 2023 (2023), pp. 1441–1444.
47. M. Zafar Iqbal, H. Fathallah, and N. Belhadj, "Optical fiber tapping: Methods and precautions," in *8th International Conference on High-capacity Optical Networks and Emerging Technologies,* (2011), pp. 164–168.
48. H. Song, R. Lin, Y. Li, *et al.*, "Machine-learning-based method for fiber-bending eavesdropping detection," Opt. Lett. **48**, 3183–3186 (2023).
49. A. K. Yilmaz, A. Deniz, and H. Yuksel, "Experimental Optical Setup to Measure Power Loss versus Fiber Bent Radius for Tapping into Optical Fiber Communication Links," in *2021 International Conference on Electrical, Computer and Energy Technologies (ICECET),* (2021), pp. 1–6.
50. Q. Lei, Y. Li, H. Song, *et al.*, "Multi-intensity Bending Eavesdropping Detection and Identification Scheme Based on the State of Polarization," in *2023 Opto-Electronics and Communications Conference (OECC),* (2023), pp. 1–4.
51. V. Spurny, P. Dejdar, A. Tomasov, *et al.*, "Eavesdropping Vulnerabilities in Optical Fiber Networks: Investigating Macro-Bending-Based Attacks Using Clip-on Couplers," in *2023 International Workshop on Fiber Optics on Access Networks (FOAN),* (2023), pp. 47–51.
52. P. M. Krummrich, D. Ronnenberg, W. Schairer, *et al.*, "Demanding response time requirements on coherent receivers due to fast polarization rotations caused by lightning events," Opt. Express **24**, 12442–12457 (2016).
53. D. Charlton, S. Clarke, D. Doucet, *et al.*, "Field Measurements of SOP transients in OPGW, with time and location correlation to lightning strikes," Opt. Express **25**, 9689–9696 (2017).
54. H. Sorensen, D. Jones, M. Heideman, and C. Burrus, "Real-valued fast Fourier transform algorithms," IEEE Trans. on Acoust. Speech, Signal Process. **35**, 849–863 (1987).
55. K. Abdelli, J. Y. Cho, F. Azendorf, *et al.*, "Machine-learning-based anomaly detection in optical fiber monitoring," J. Opt. Commun. Netw. **14**, 365–375 (2022).
56. K. Abdelli, M. Lonardi, J. Gripp, *et al.*, "Anomaly Detection and Localization in Optical Networks Using Vision Transformer and SOP Monitoring," in *2024 Optical Fiber Communications Conference and Exhibition (OFC),* (2024), pp. 1–3.
57. L. Sadighi, S. Karlsson, C. Natalino, and M. Furdek, "Machine Learning-Based Polarization Signature Analysis for Detection and Categorization of Eavesdropping and Harmful Events," in *2024 Optical Fiber Communications Conference and Exhibition (OFC),* (2024), pp. 1–3.
58. P. D. Hernández, J. A. Ramírez, and M. A. Soto, "Deep-Learning-Based Earthquake Detection for Fiber-Optic Distributed Acoustic Sensing," J. Light. Technol. **40**, 2639–2650 (2022).
59. E. R. Martin, F. Huot, Y. Ma, *et al.*, "A Seismic Shift in Scalable Acquisition Demands New Processing: Fiber-Optic Seismic Signal Retrieval in Urban Areas with Unsupervised Learning for Coherent Noise Removal," IEEE Signal Process. Mag. **35**, 31–40 (2018).